materials

MDPI

Article

Cobalt Impregnation on Titania Photocatalysts Enhances Vis Phenol Photodegradation

Soukayna Belekbir [1], Mohammed El Azzouzi [1], Laura Rodríguez-Lorenzo [2], Adnane El Hamidi [1], Juan Arturo Santaballa [3,*] and Moisés Canle [3,*]

[1] Laboratory of Nanomaterials, Nanotechnologies and Environment, Center of Materials Science, Faculty of Sciences, Mohammed V University in Rabat, Rabat BP 1014, Morocco
[2] INL—International Iberian Nanotechnology Laboratory, Water Quality Group, Av. Mestre José Veiga, 4715-330 Braga, Portugal
[3] React! Group, Department of Chemistry, Faculty of Sciences & CICA, University of A Coruña, E-15071 A Coruña, Spain
* Correspondence: arturo.santaballa@udc.es (J.A.S.); moises.canle@udc.es (M.C.)

Abstract: One of the main challenges of photocatalysis is to find a stable and effective photocatalyst, that is active and effective under sunlight. Here, we discuss the photocatalytic degradation of phenol as a model pollutant in aqueous solution using NUV-Vis (>366 nm) and UV (254 nm) in the presence of TiO_2-P25 impregnated with different concentrations of Co (0.1%, 0.3%, 0.5%, and 1%). The modification of the surface of the photocatalyst was performed by wet impregnation, and the obtained solids were characterized using X-ray diffraction, XPS, SEM, EDS, TEM, N_2 physisorption, Raman and UV-Vis DRS, which revealed the structural and morphological stability of the modified material. BET isotherms are type IV, with slit-shaped pores formed by nonrigid aggregate particles and no pore networks and a small H3 loop near the maximum relative pressure. The doped samples show increased crystallite sizes and a lower band gap, extending visible light harvesting. All prepared catalysts showed band gaps in the interval 2.3–2.5 eV. The photocatalytic degradation of aqueous phenol over TiO_2-P25 and Co(X%)/TiO_2 was monitored using UV-Vis spectrophotometry: Co(0.1%)/TiO_2 being the most effective with NUV-Vis irradiation. TOC analysis showed ca. 96% TOC removal with NUV-Vis radiation, while only 23% removal under UV radiation.

Keywords: photocatalysis; phenol; cobalt; oxygen vacancies; UV-Vis radiation (366 nm); UV (254 nm); TiO_2-P25; wet impregnation; SERS

Citation: Belekbir, S.; El Azzouzi, M.; Rodríguez-Lorenzo, L.; El Hamidi, A.; Santaballa, J.A.; Canle, M. Cobalt Impregnation on Titania Photocatalysts Enhances Vis Phenol Photodegradation. *Materials* **2023**, *16*, 4134. https://doi.org/10.3390/ma16114134

Academic Editor: Rodica Zavoianu

Received: 21 March 2023
Revised: 15 May 2023
Accepted: 23 May 2023
Published: 1 June 2023

1. Introduction

Many activities, such as agriculture, medicine, or industry, release pollutants into the environment, creating one of the most serious problems we currently face: environmental pollution. Water pollution, in particular, poses important risks to human health and the environment. Therefore, the control of pollutants released into aqueous media has led to increasingly restrictive environmental regulations. Phenol is considered a major pollutant because of its toxicity, bioaccumulation, low biodegradability, and carcinogenicity [1]. It causes an unpleasant taste and odor in drinking water [2], and it is harmful to living organisms at low concentrations, toxic and mutagenic, being absorbed through the skin at high concentrations [3]. The main sources of anthropogenic phenols in the aquatic environment are wastewaters from manufactures of resins, chemicals, dyes, polymers, pesticides, coal conversion, and petrochemical industries [4].

Considerable efforts have been devoted to developing approaches aiming to a complete removal of organic pollutants. However, the application of conventional methods, such as membrane filtration, adsorption on activated carbon, ion exchange on synthetic resins, purification by chemical coagulation systems, etc., are not cost effective and may generate wastes that require further treatment stages and additional costs [5,6]. Conversely,

photocatalysis requires low cost and abundant chemicals, at little or no energy expense, and can operate autonomously [7], requiring only light (Visible and/or UV) and a semiconductor catalyst to achieve or accelerate chemical reactions [8–13]. Though a number of photocatalysts have been studied (Al_2O_3, ZnO, Fe_2O_3, and TiO_2) [14], the most widely used one is TiO_2, of which the photoactive forms are anatase and rutile. One of the most effective forms, and by far the most widely used, is a mixture of anatase/rutile at a ratio of ca. 80%/20%, with a small percentage of amorphous form, commercialized as Evonik-P25 (referred to here as P25) [15]. The improved photocatalytic activity of P25 is attributed to its junction, which reduces the e^-/h^+ recombination [16]. TiO_2-P25 is known for its lack of toxicity when presented as aggregates or macroparticles, chemical stability in aqueous solution, and low cost [17]. Despite all these advantages, its use remains limited because of its high band-gap energy, 3.2 eV, thus limiting its photocatalytic activity to the UV region, which represents only 4 to 5% of the solar spectrum.

Numerous strategies have been used to increase the photocatalytic efficiency of TiO_2-P25 under Vis irradiation, including doping/loading with metal ions or nonmetals [18,19]. Doping allows a reduction in the e^-/h^+ recombination and decreases the band gap, shifting the photocatalyst light absorption towards the Vis region, which facilitates the use of sunlight as the irradiation source [20]. Recently, a number of papers have been devoted to the photodegradation of phenolic compounds [21]; many of them related to the application of TiO_2 as a photocatalyst [22,23]. Co(II)-doped TiO_2 was found to have high photocatalytic activity for the degradation of acetaldehyde [24], 2-chorophenol [25], azo dyes [26], and even exhibited antimicrobial features [27].

Here, we present an unprecedented extensive study of phenol photodegradation under UV and near-visible light irradiation, using TiO_2-P25 (Degussa) loaded with Co ions at different concentrations (Co(X%)/TiO_2, where X = 0.1%, 0.3%, 0.5%, and 1%). The samples were prepared by the wet impregnation method. Extensive characterization of the samples was carried out using X-ray diffraction (XRD), SEM, EDS, TEM, X-ray photoelectron spectroscopy (XPS), Raman and UV-Vis diffuse reflectance spectroscopy (UV-Vis DRS), and N_2 physisorption. Its photocatalytic activity was evaluated by monitoring phenol transformation, taken as a model organic pollutant, and total organic carbon (TOC) evolution. The photoreaction was conducted in an aqueous solution under near-UV light at wavelengths of 366 nm and longer and also under UV light (254 nm).

2. Experimental Procedure

2.1. Materials

TiO_2-P25 was from Evonik (ca. 70:30% anatase:rutile with a small amount of amorphous phase): surface area of 55 ± 15 $m^2 \cdot g^{-1}$ [28] and particle size of ∼30 nm [29]. Cobalt (II) sulfate heptahydrate ($CoSO_4 \cdot 7H_2O$, ≥97%) was from Aldrich, and phenol (C_6H_5OH, 99.5%) from Sigma. Acetonitrile (HPLC grade) was from J.T. Baker. O_2 gas (purity ≥ 99.995%) was used in some experiments. All chemicals were used without further purification. Distilled water was obtained from a Millipore apparatus (Milli-Q water), resistivity of 18.2 MΩ at 298.0 K and total organic carbon (TOC) less than 5 $\mu g \cdot L^{-1}$.

2.2. Catalyst Synthesis

Wetness impregnation was used to immobilize Co(II) on the surface of TiO_2 nanoparticles to prepare Co/TiO_2 photocatalysts [30] with enhanced photocatalytic properties. $CoSO_4 \cdot 7H_2O$ was dissolved in distilled water and impregnated on Degussa TiO_2-P25 nanoparticles under vigorous stirring.

This suspension was stirred for 24 h, and then dried in an oven at 50 °C to dry it completely. Then, the photocatalysts were calcined in a furnace (Paragon model HT-22D, Thermcraft) at 600 °C for 4 h with a ramp rate of 10 $°C \cdot min^{-1}$. Finally, the so-prepared catalysts were ground thoroughly and labeled as Co(X%)/TiO_2, where X denotes the Co(II) mass percent relative TiO_2, X = 0.1%, 0.3%, 0.5%, and 1%. TiO_2 particles turned from white to yellowish as the cobalt percentage increased.

The samples were placed in water under stirring for 2 h to test for potential Co^{n+} leaching; after filtration, the solution was analyzed using ICP/MS and the dry solid by XRD. No evidence of Co^{n+} leaching was found (Table 1).

Table 1. Co(II) percent in Co/TiO_2 catalysts after 2 h stirring in water.

Starting material	0.1000%	0.3000%	0.5000%	1.0000%
After 2 h	0.0995%	0.2950%	0.5053%	1.0180%

2.3. Characterization

X-ray diffraction (XRD) measurements were conducted with a Bruker Siemens D5000 diffractometer following Bragg–Brentano geometry and θ/2θ configuration and equipped with a graphite monochromator. The optics consist of primary and secondary 2° Soller slots, a variable output slot, a 1mm receiver slot, a 0.2 mm monochromator slot, and a 0.6 mm detector slot. The detector was a scintillation counter. The acquisition conditions were a sweep range (2θ): 2–80°, a jump size (step): 0.050°, and the acquisition time at each jump was about 2.5 s (time per jump). The DiffracPlus software v. 8.0.0.2 (Socabim) was used for data processing.

The morphology of TiO_2-P25 and $Co(X\%)/TiO_2$ were studied using a Jeol JSM-IT100 scanning electron microscope (SEM) equipped with an energy dispersive X-ray (EDX) system to obtain information on the surface elemental composition. The samples were deposited on thin films of amorphous carbon and coated with gold (2 nm). Transmission electron microscopy (TEM), using a Jeol JEM 1100 instrument, operating at an acceleration voltage of 80 kV, was also employed to examine the photocatalysts' surface morphology. Samples were prepared by depositing a few drops of nanoparticle suspension on carbon-coated copper grids (electron microscopy, 200 mesh) and air drying.

Textural characterization was carried out using adsorption/desorption isotherms of N_2, as adsorption gas, at 77.4 K (Tristar II Plus—Micromeritics, automatic station with 3 simultaneous measurement ports). Helium was used for the measurement of the dead volume of the sample holders. Isotherms were measured in the range $P/P_0 = 0.1–1.0$. The range of the BET area used for the calculation of the specific surface area was $P/P_0 = 0.05–0.3$. "Microactive for Tristar II Plus", v.2.03 (Micromeritics), was the software for control, acquisition, and data processing.

Raman measurements of the dried samples on glass were performed using a Witec Alpha 300 R confocal Raman system equipped with 633 and 785 nm excitation laser lines and a grating of 600 $gr{\cdot}cm^{-1}$. Raman spectra were acquired at room temperature using a 20× objective over the spectra range of 90–2500 and 90–1800 cm^{-1} for 633 and 785 nm, respectively, laser powers at the samples of 21 mW (633 nm), 28 and 35 mW (785 nm), and acquisition times in the range of 0.5–5 s with 10 accumulation. The Raman spectra were processed with the Project5.2 Witec software for peak assignment including position, height, and FWHM. SpectraGryph 1.2 software was used for spectral processing involving baseline, background removal (i.e., Raman spectrum of glass was subtracted for the spectra acquired using a 785 nm laser line), and cosmic ray removal correction. Raman shift calibration was performed using a silicon wafer (peak at 520 cm^{-1}). The spectra were normalized to the E_g peak (146 cm^{-1}) for a better comparison between samples.

$Co(0.1\%)/TiO_2$ photocatalyst was analyzed by X-ray photoelectron spectroscopy (XPS) using a Thermo Scientific K-Alpha ESCA instrument equipped with an Al Kα monochromatized radiation (hν = 1486.7 eV) X-ray source. Measurements were carried out in a Constant Analyzer Energy mode with a 100 eV pass energy for survey spectra, and 20 eV pass energy for high-resolution spectra. The spot size selected was 400 μm and K-Alpha's charge compensation system was employed during analysis. In data analysis, C 1s = 285.0 eV was taken as the binding energy reference. Surface elemental composition was determined using the standard Scofield photoemission cross sections.

The UV-Vis diffuse reflectance spectra (DRS) (200–800 nm) of the solid photocatalyst was measured on a JASCO V-560 UV-Vis spectrophotometer with a double monochromator

and double beam optical system, equipped with an integrating sphere attachment (JASCO ISV-469, Oklahoma City, OK, USA). Reflectance spectra were converted to equivalent absorption Kubelka–Munk units.

2.4. Photocatalytic Activity

The photocatalytic activity of the synthetized samples was tested in an axial photoreactor, under UV and near-UV-Vis light (NUV-Vis), monitoring changes in phenol (C_6H_5OH) concentration in aqueous solution. Two types of photocatalytic experiments were carried out. The first was performed under NUV-Vis light, in which the photoreactor was equipped with a Heraeus TQ 150 medium-pressure Hg-vapor lamp, with intense emission lines at 254, 313, 366, 405, 436, 546, and 578 nm. A Duran 50® glass jacket, filled with water, was used to cut off the radiation below 366 nm. For the second experiment, the photoreactor was equipped with a Heraeus TNN 15/32 low-pressure Hg-vapor lamp, with a single intense emission line at 254 nm, located inside a quartz tube. The photon flux at 366 nm, as determined by potassium ferrioxalate actinometry, [31] was 2.38×10^{-6} Einstein·s^{-1}, and at 254 nm, it was of 8.33×10^{-8} Einstein·s^{-1}.

The photocatalytic reactions were performed under a coherent magnetic stirring of 200 mL phenol solution, with an initial concentration of 50 mg·L^{-1} to facilitate monitoring, mixed with 200 mg of photocatalyst under controlled O_2 pressure. All samples were kept in the dark for 30 min, to ensure adsorption–desorption equilibrium. The heterogeneous suspensions, at natural pH, were exposed to UV irradiation for 60 min and to NUV-Vis irradiation for 300 min at ca. 25 °C, maintained by water flow from a thermostat-cryostat. Samples of aqueous phenol and photocatalysts were taken at time intervals and filtered through Sartorius NY 0.45 ™ filters.

Phenol concentration was monitored using a Biochrom Libra S70 spectrophotometer to measure the UV-Vis absorbance at 270 nm and using HPLC UV-Vis at 210 and 270 nm, in a Thermo Fisher instrument equipped with a 6000 LP UV detector, an AS 3000 autosampler, and a P4000 solvent pump. A KROMAPHASE C18 column (4.6 mm × 150 mm × 5 µm) was used, with a volume of 50 µL injected, a flow rate of 1.0 mL·min^{-1}, at 30 °C, the mobile phase being acetonitrile and water (25:75, v/v). Replicate experiments showed differences in rate constants within 5% error.

Total organic carbon (TOC) removal was measured using a ShimadzuTOC-5000A analyzer. Photoproducts were identified using HPLC/MS (Thermo Scientific LTQ Orbitrap Discovery), equipped with an electrospray interface operating in negative ion mode (ESI-), with a Phenomenex Kinetex XB-C18 column (100 mm × 2.6 µm) operating at 30 °C with elution solvents A (0.1% formic acid) and C (0.1% methanol) at a flow rate of 200 µL·min^{-1}. The gradient followed was 0–1 min, 95–95% of A and 5–5% of C; 1–8 min, 95–5% A and 5–95% C; 8–10 min, 5–5% A and 95–95% C; 10–11 min, 5–95% of A and 95–5% C; and 11–15 min, 95–95% A and 5–5% C. The amount injected was 5–25 µL. The analyses were carried out using full-scan data-dependent MS scanning from m/z 50 to 500. The obtained photoproducts were the same found in the photocatalyzed degradation of phenol using surface-impregnated TiO_2 (M = Cu, Cr or V) as photocatalysts [32].

3. Results and Discussion

3.1. Characterization of the Catalysts

3.1.1. X-ray Diffraction

The crystal structure of the synthesized samples was evaluated using XRD analysis, and the results are shown in Figure 1. Pure TiO_2-P25 shows eight primary peaks at 25.20°, 36.52°, 37.78°, 48.00°, 53.96°, 56.86°, 62.74°, and 75.08°, which are assigned to anatase diffraction planes: (1 0 1), (1 0 3), (0 0 4), (2 0 0), (1 0 5), (2 1 1), (2 0 4), and (2 1 5). The four peaks located at 27.34°, 36.02°, 41.14°, and 55.00° can be attributed to rutile diffraction planes: (1 1 0), (1 0 1), (1 1 1), and (2 1 1) [33]. The diffraction patterns of Co(0.1%)/TiO_2, Co(0.3%)/TiO_2, Co(0.5%)/TiO_2, and Co(1%)/TiO_2 photocatalysts were very similar to that of nonimpregnated TiO_2-P25. No other metal and/or metal oxides were observed,

and the results are shown in Figure 1. Pure TiO_2-P25 shows eight primary peaks at 25.20°, 36.52°, 37.78°, 48.00°, 53.96°, 56.86°, 62.74°, and 75.08°, which are assigned to anatase diffraction planes: (1 0 1), (1 0 3), (0 0 4), (2 0 0), (1 0 5), (2 1 1), (2 0 4), and (2 1 5). The four peaks located at 27.34°, 36.02°, 41.14°, and 55.00° can be attributed to rutile diffraction planes: (1 1 0), (1 0 1), (1 1 1), and (2 1 1) [33]. The diffraction patterns of Co(0.1%)/TiO_2, Co(0.3%)/TiO_2, Co(0.5%)/TiO_2, and Co(1%)/TiO_2 photocatalysts were very similar to that of nonimpregnated TiO_2-P25. No other metal and/or metal oxides were observed, which could be related to the low Co content (0.1%, 0.3%, 0.5%, and 1% by weight) and its uniform distribution onto the TiO_2 surface [30]. Table 2 shows the crystalline phase percentage of anatase and rutile calculated from their most intense reflections (1 0 1) and (1 1 0), respectively, using the Spurr and Myers equation [34]. The anatase to rutile ratio decreases when going from P25 [35] to Co(X%)/TiO_2 due to the dopant Co^{2+} promoting anatase to rutile phase transformation [16].

which could be related to the low Co content (0.1%, 0.3%, 0.5%, and 1% by weight) and its uniform distribution onto the TiO_2 surface [30]. Table 2 shows the crystalline phase percentage of anatase and rutile calculated from their most intense reflections (1 0 1) and (1 1 0), respectively, using the Spurr and Myers equation [34]. The anatase to rutile ratio decreases when going from P25 [35] to Co(X%)/TiO_2 due to the dopant Co^{2+} promoting anatase to rutile phase transformation [16].

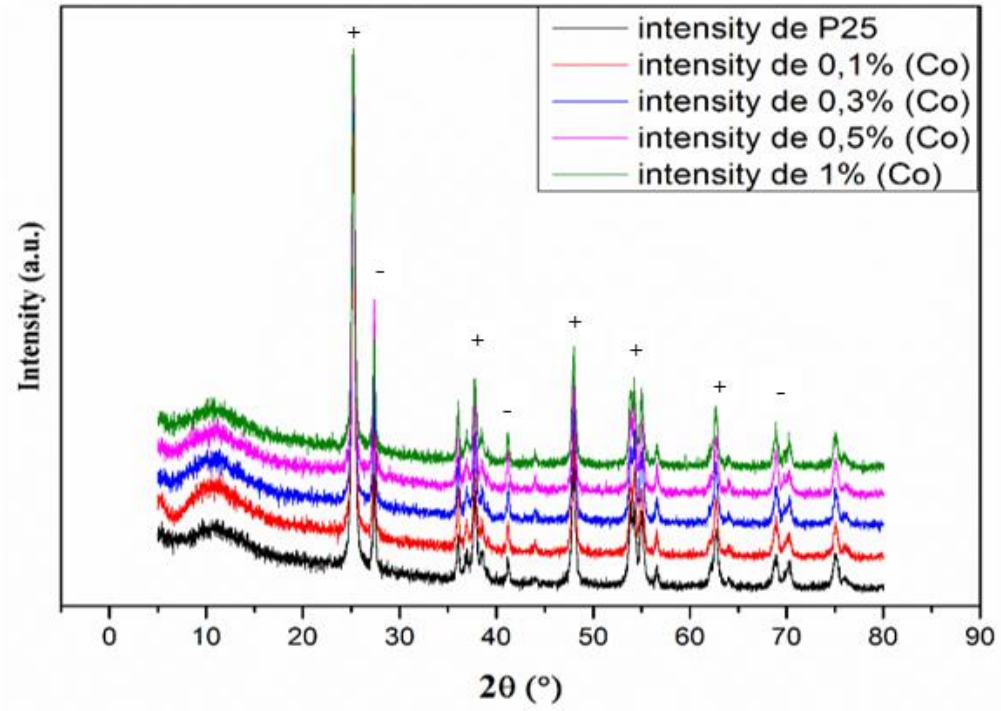

Figure 1. X-ray diffraction patterns of pure TiO_2-P25 and Co/TiO_2 samples with different Co/Ti ratio (+ anatase, - rutile).

Table 2. Crystalline phase percentage, anatase and rutile main reflections (2θ), crystallite size (Scherrer), and unit cell parameters (tetragonal) from XRD analysis of P25 and Co(X%)/TiO_2.

	Parameter	P25	Co(0.1%)	P25	Co(0.1%) [a]	Co(0.3%)	Co(0.5%)	Co(1.0%)
Anatase	wt%	75	69	75	70	68	63.5	71
	Crystallite size (nm)	21.99	26.37	21.99	26.37	25.05	26.93	24.70
	a = b (nm)	0.3800	0.3796	0.3800	0.3796	0.3796	0.3796	0.3795
	c (nm)	0.9449	0.9490	0.9522	0.9530	0.9473	0.9473	0.9486
Rutile	wt%	25	31	25	30	32	36.5	29
	Crystallite size (nm)	31.43	36.58	31.43	34.20	38.96	30.13	32.40
	a = b (nm)	0.4610	0.4606	0.4610	0.4603	0.4583	0.4603	0.4603
	c (nm)	0.2962	0.2961	0.2956	0.2952	0.2966	0.2966	0.2963

[a] After stirring in water for two hours.

The substitution of Ti^{4+} by Co^{2+}, with slightly different size, induces a charge imbalance which implies the creation of oxygen vacancies to maintain charge neutrality [36]. Co^{2+} and oxygen vacancies introduce defect levels acting as trapping sites, therefore diminishing electron–hole recombination [37]. Effect levels imply the presence of interband states which means a reduction in the band gap, boosting the photocatalytic activity under Vis radiation.

Crystallite size was calculated using the Scherrer equation [38]. The observed trend with both polymorphs is to increase in size continuously from TiO_2-P25 to the doped photocatalyst, with a tendency to reduce in size as the doping percentage increases. A similar behavior has been reported for rutile [39]. Doping, within the used percentages, does not affect cell parameters (Table 2), which is consistent with the substitution of

interband states which means a reduction in the band gap, boosting the photocatalytic activity under Vis radiation.

Crystallite size was calculated using the Scherrer equation [38]. The observed trend with both polymorphs is to increase in size continuously from TiO_2-P25 to the doped photocatalyst, with a tendency to reduce in size as the doping percentage increases. A similar behavior has been reported for rutile [39]. Doping, within the used percentages, does not affect cell parameters (Table 2), which is consistent with the substitution of Ti^{4+} by Co^{2+} in the doped photocatalyst, provided they show relatively similar radii (74.5 *vs.* 79 pm, respectively, considering low spin Co^{2+} and 6-coordination) [40]. The fact that cell parameters are not affected is in agreement with doping taking place mainly on the surface and not on the bulk.

As stated above, 1 g of a $Co(0.1\%)/TiO_2$ sample in 1 L of distilled water was stirred for 2 h. The solid recovered after filtration and drying was XRD analyzed. The same diffraction peaks of $Co(0.1\%)/TiO_2$ were found before and after the test (Figure S1 of Supplementary Materials); therefore, similar values were obtained for the derived parameters, thus confirming the stability of the as-prepared photocatalyst.

3.1.2. Raman Spectroscopy

Figure 2 shows the Raman spectra of $Co(0.1\%)/TiO_2$, which are compared with the Raman spectrum of undoped TiO_2, acquired using two different lasers, 633 and 785 nm, and two laser powers. Anatase polymorph, a tetragonal structure, is present. The Raman active "lattice vibrations" shown in Table 3 are assigned based on the D_{4h} point group.

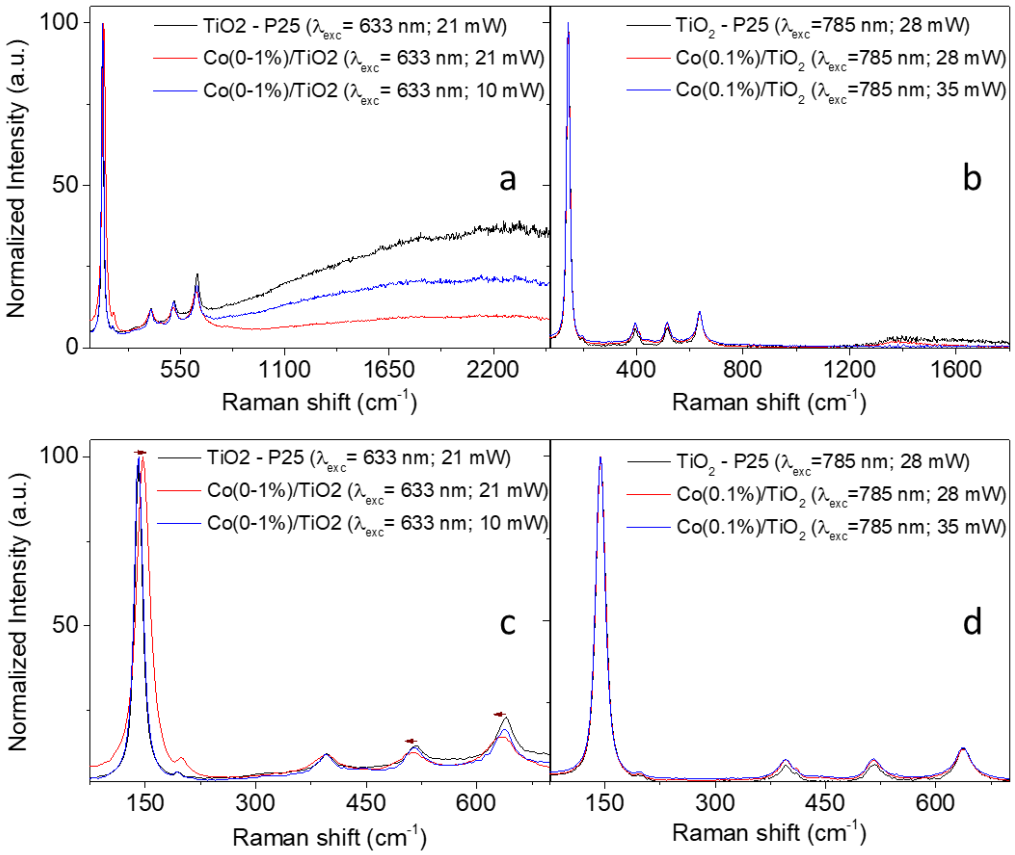

Figure 2. Raman spectra of $Co(0.1\%)/TiO_2$ photocatalyst acquired using (**a**) 633 nm and (**b**) 785 nm excitation lasers. Two different laser powers were used: 21 and 10 mW for 633 nm and 28 and 35 mW for 785 nm. Spectra shown in (**c**,**d**) are centered in a smaller spectra window (90 to 670 cm^{-1}) for a better observation of the Raman peaks corresponding to the anatase phase.

The very low intensity band at ca. 445 cm^{-1}, E_g mode of the rutile phase, does not allow a rough estimation of the weight ratios of anatase phase to rutile phase from the Raman spectrum. The table also includes Ti-O and Ti-Ti bond lengths calculated using covalence/length/frequency relations [41]. Values obtained for $Co(0.1\%)/TiO_2$ are similar to those reported for P25, which agrees with the tiny structural effect of 0.1% Co doping observed using XRD.

Table 3. Raman active "lattice vibrations" for anatase in P25 [38] and in Co(0.1%)/TiO_2, Ti-Ti bond lengths (octahedral chain) and Ti-O bond lengths.

Mode	Photocatalyst	Vibration Wavenumber (cm^{-1}) and Bond Length (Å)		
E_g	P25	143 (d_{Ti-Ti}: 2.85)	196 (d_{Ti-Ti}: 2.65)	638 (d_{Ti-O}: 2*x* 1.89)
	P25 (this work)	144 (d_{Ti-Ti}: 2.85)	198 (d_{Ti-Ti}: 2.64)	638 (d_{Ti-O}: 2*x* 1.89)
	Co(0.1%)/TiO_2	144 (d_{Ti-Ti}: 2.85)	197 (d_{Ti-Ti}: 2.65)	637 (d_{Ti-O}: 2*x* 1.89)
B_{1g}	P25	396 (d_{Ti-O}: 3*x* 2.20)		
	P25 (this work)	396 (d_{Ti-O}: 3*x* 2.20)		
	Co(0.1%)/TiO_2	395 (d_{Ti-O}: 3*x* 2.20)		
A_{1g}	P25	515 (d_{Ti-O}: 3*x* 2.03)		
	P25 (this work)	518 (d_{Ti-O}: 3*x* 2.02)		
	Co(0.1%)/TiO_2	515 (d_{Ti-O}: 3*x* 2.03)		

The method of preparation of the doped photocatalysts determines its particle size, which has to do with oxygen vacancies and electron–phonon coupling. Both factors may influence shifts and broadening of Raman peaks. Contrary to Co-doped TiO_2 synthetized using sol-gel [42], the as-prepared photocatalyst does not show a wavenumber shift upon the excitation of 785 nm laser line at any of the power laser values used. The FWHW of the most intense peak is the same for the undoped and doped (Co(0.1%)/TiO_2) sample (Figure 2d, Table S1), the corresponding phonon lifetime being 0.34 ps. Interestingly, a red shift of 6 cm^{-1} was observed in the peak centered at 141 cm^{-1}, while the peaks centered at 517 and 640 cm^{-1} displayed a blue shift of 4–5 cm^{-1} (Figure 2c and Table S1 for peak at 141 cm^{-1}) upon the excitation of 633 nm with a laser power of 21 mW. However, these shifts were not observed at lower powers of the 633 nm laser (Figure 2c,d, Table S1 for peak at 141 cm^{-1}). This laser-induced phase transition (*e.g.*, low crystallinity or phase transformation) in Co-doped anatase TiO_2 nanoparticles was previously reported [43]. This laser power dependence was not observed with the 785 nm laser line since its energy is lower than that of the 633 nm one.

Figure S2 shows that the intensity of the well-defined peaks is higher for the Co-doped photocatalyst using both laser lines (see Table S1 for the most intense peak in Supplementary Materials), such enhancement has been previously described [44,45].

3.1.3. Scanning Electron Microscopy and Energy Dispersive Spectroscopy

The morphology and elemental analysis of the Co(X%)/TiO_2 samples were studied using scanning electron microscopy/energy dispersion spectroscopy (SEM/EDS). SEM images, Figure 3, show the crystals' shape and size of all cobalt-loaded samples are similar to those of unmodified P25-TiO_2 [17], with an average crystal size of 30 nm, in agreement with the value obtained from XRD data (vide supra). EDS analysis shows the percent of cobalt matches the initial doped amount at the lowest percentages, while at higher Co/TiO_2 doping percentages, the presence of Co is lower on the surface (Table 4), which could be attributed to Co ions diffusing into inner layers of the photocatalyst, a process that is facilitated by oxygen vacancies. The EDS-mapping images of the doped photocatalysts' surfaces revealed a homogeneous distribution of cobalt ions [35]. Considering typical penetrations of X-rays in SEM/EDS, the Co ions reached depths of not less than 2 µm below the surface. The presence of Co with an optimal concentration (0.1%) prevents the TiO_2-P25 particles from agglomerating, probably due to the development of a surface charge. Large aggregates can decrease photocatalytic activity by reducing the exposed surface and shading active sites from exciting radiation [23].

photocatalysts' surfaces revealed a homogeneous distribution of cobalt ions [35]. Considering typical penetrations of X-rays in SEM/EDS, the Co ions reached depths of not less than 2 µm below the surface. The presence of Co with an optimal concentration (0.1%) prevents the TiO_2-P25 particles from agglomerating, probably due to the development of a surface charge. Large aggregates can decrease photocatalytic activity by reducing the exposed surface and shading active sites from exciting radiation [23].

Table 4. Cobalt weight percent content for Co(X%)-TiO_2 samples by EDS analysis.

Sample	Co(0.1%)/TiO_2	Co(0.3%)/TiO_2	Co(0.5%)/TiO_2	Co(1%)/TiO_2
Co (Weight %)	0.11	0.29	0.46	0.69

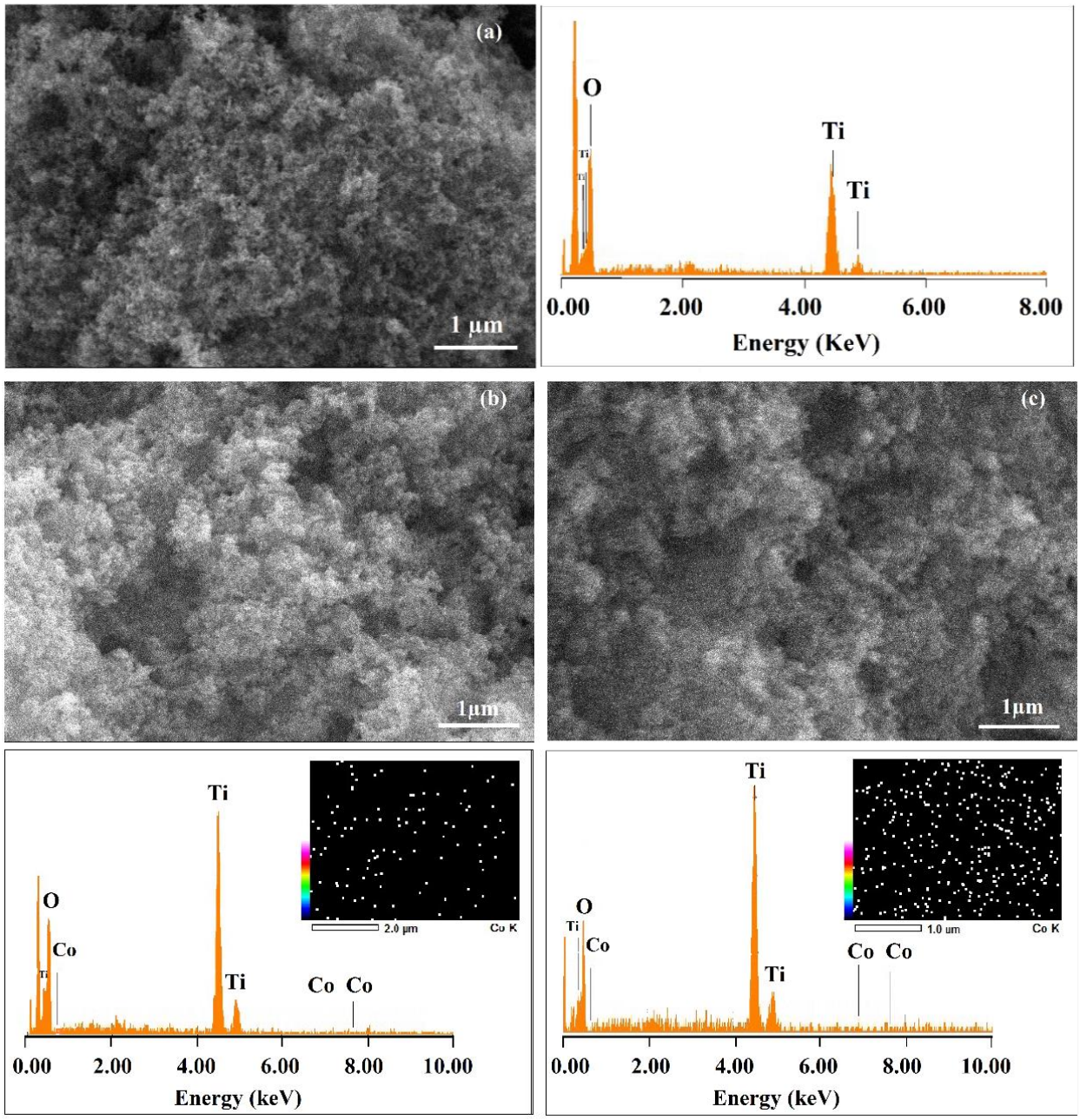

Figure 3. *Cont.*

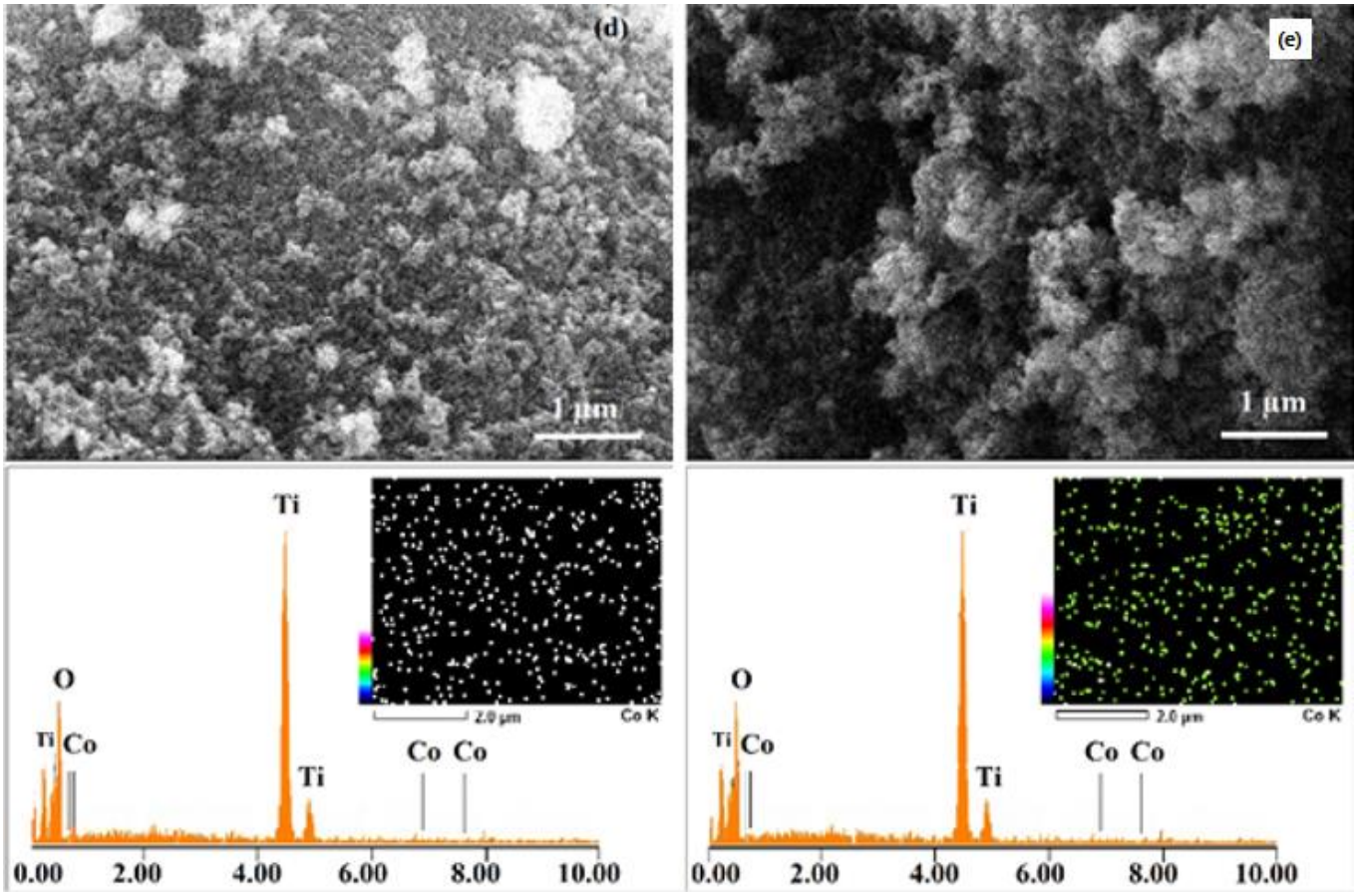

Figure 3. SEM/EDS micrographs of (**a**) TiO_2-P25 and Co(X%)/TiO_2 samples as (**b**) Co(0.1%)/TiO_2, (**c**) Co(0.3%)/TiO_2, (**d**) Co(0.5%)/TiO_2, (**e**) Co(0.5%)/TiO_2.

Table 4. Cobalt weight percent content for Co(X%)-TiO_2 samples by EDS analysis.

Sample	Co(0.1%)/TiO_2	Co(0.3%)/TiO_2	Co(0.5%)/TiO_2	Co(1%)/TiO_2
Co (Weight %)	0.11	0.29	0.46	0.69

3.1.4. XPS Analysis

Co(X%)/TiO_2 samples were analyzed using XPS, in an attempt to understand the bonding states of the surface elements on the doped photocatalyst. The survey XPS spectrum is shown in Figure 4. The atomic composition of C 1s, Ti 2p, O 1s, and Co 2p of the Co/TiO_2 photocatalyst was 27.8%, 20.1%, 50.3%, and 1.8%, respectively. The characteristic satellite (shake up) of Co at around 786 eV is evidence of the presence of Co(II). The high-resolution Co 2p spectrum showed spin-orbit splitting into $2p_{1/2}$ and $2p_{3/2}$ components (Figure S2a). The Co 2p spectrum is close, or quite similar, to the $Co(OH)_2$ compound [46]. The dominant Ti $2p_{3/2}$ peak is located at 458.8 eV binding energy and Ti $2p_{1/2}$ at 464.5 eV, i.e., with a spin-orbit splitting value of 5.7 eV, corresponding to Ti(IV) [47], Figure S2b. XPS Ti 2p peaks appear at slightly higher binding energy than in the case of P25 (458.6 and 464.2 eV, respectively). Electron density is transferred from Ti(IV) to Co(II), due to the higher Pauling electronegativity of the latter, and the binding energy increases. The peak at ca. 530 eV (O 1s, Figure S2c) is characteristic of the Ti–O lattice bond of TiO_2 [48].

3.1.4. XPS Analysis

Co(X%)/TiO_2 samples were analyzed using XPS, in an attempt to understand the bonding states of the surface elements on the doped photocatalyst. The survey XPS spectrum is shown in Figure 4. The atomic composition of C 1s, Ti 2p, O 1s, and Co 2p of the Co/TiO_2 photocatalyst was 27.8%, 20.1%, 50.3%, and 1.8%, respectively. The characteristic satellite (shake up) of Co at around 786 eV is evidence of the presence of Co(II). The high-resolution Co 2p spectrum showed spin-orbit splitting into $2p_{1/2}$ and $2p_{3/2}$ components (Figure S2a). The Co 2p spectrum is close, or quite similar, to the $Co(OH)_2$ compound [46]. The dominant Ti $2p_{3/2}$ peak is located at 458.8 eV binding energy and Ti $2p_{1/2}$ at 464.5 eV, i.e., with a spin-orbit splitting value of 5.7 eV, corresponding to Ti(IV) [47], Figure S2b. XPS Ti 2p peaks appear at slightly higher binding energy than in the case of P25 (458.6 and 464.2 eV, respectively). Electron density is transferred from Ti(IV) to Co(II), due to the higher Pauling electronegativity of the latter, and the binding energy increases. The peak at ca. 530 eV (O 1s, Figure S2c) is characteristic of the Ti–O lattice bond of TiO_2 [48].

Materials **2023**, *16*, x FOR PEER REVIEW 10 of 18

Materials **2023**, *16*, 4134 10 of 18

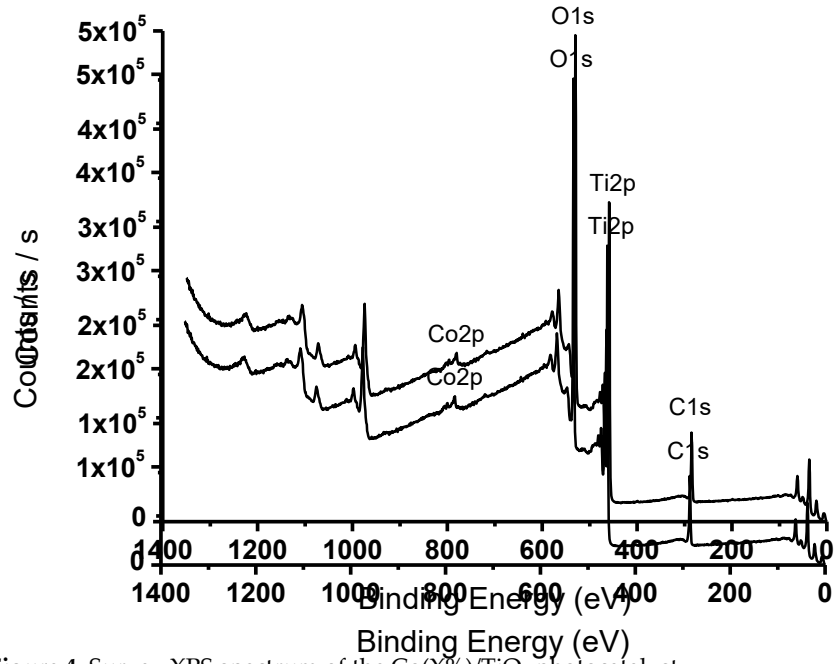

Figure 4. Survey XPS spectrum of the Co(X%)/TiO_2 photocatalyst.

Figure 4. Survey XPS spectrum of the Co(X%)/TiO_2 photocatalyst.

3.1.5. Textural Properties

3.1.5. Textural Properties

The N_2 adsorption–desorption isotherm of Co(0.1%)/TiO_2 is displayed in Figure 5, which according to the IUPAC classification belongs to type IV with a very small hysteresis loop H3 (ca. 0.42–0.97 P/P0), suggesting the mesoporous nature of the photocatalyst [49]. The adsorption isotherm does not level off at high pressure, which implies the existence of slit-shaped pores formed by nonrigid aggregate particles and no pore networks according to BJH [50].

The N_2 adsorption–desorption isotherm of Co(0.1%)/TiO_2 is displayed in Figure 5, which according to the IUPAC classification belongs to type IV with a very small hysteresis loop H3 (ca. 0.42–0.97 P/P0), suggesting the mesoporous nature of the photocatalyst [49]. The adsorption isotherm does not level off at high pressure, which implies the existence of slit-shaped pores formed by nonrigid aggregate particles and no pore networks according to BJH [50].

The N_2 adsorption–desorption isotherm of Co(0.1%)/TiO_2 is displayed in Figure 5, which according to the IUPAC classification belongs to type IV with a very small hysteresis loop H3 (ca. 0.42–0.97 P/P0), suggesting the mesoporous nature of the photocatalyst [49]. The adsorption isotherm does not level off at high pressure, which implies the existence of slit-shaped pores formed by nonrigid aggregate particles and no pore networks according to BJH [50].

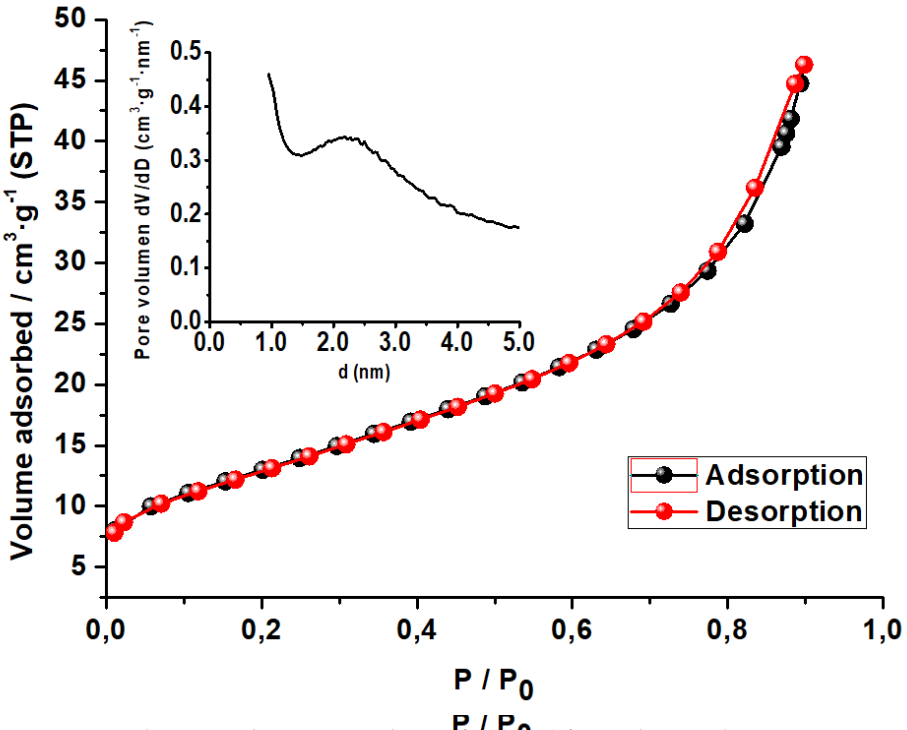

Figure 5. N_2 adsorption–desorption isotherm of Co(0.1%)/TiO_2 photocatalyst. Inset: pore size distribution.

Figure 5. N_2 adsorption–desorption isotherm of Co(0.1%)/TiO_2 photocatalyst. Inset: pore size distribution.

Figure 5. N_2 adsorption–desorption isotherm of Co(0.1%)/TiO_2 photocatalyst. Inset: pore size distribution.

The BET isotherm was used to calculate the surface area (SBET—multipoint), and the textural properties were analyzed based on the Barrett, Joyner, and Halenda (BJH) model [50] (Table 5). The observed texture is different from that of Co(0.1%/TiO_2) as prepared by the hydrothermal method, where the isotherm, also type IV, shows a large H3 hysteresis loop (0.4–0.8 P/P_0), and the reported values of SBET (22.8 $m^2 \cdot g^{-1}$) and pore volume (0.033 $cm^3 \cdot g^{-1}$) are smaller than those of the as-synthesized photocatalyst [51]. Pore size distribution shows a maximum at 22 Å, just in the lower mesopore limit.

Table 5. Textural properties of Co(0.1%)/TiO_2.

Photocatalyst		**Co(0.1%)/TiO_2**		
BET	$S_{BET}/m^2 \cdot g^{-1}$	39.58 ± 0.07		
	Constant C	102.83		
	V_m (monolayer adsorption volume)/$cm^3 \cdot g^{-1}$	9.09		
Parameter		Surface area ($m^2 \cdot g^{-1}$)	Pore volume ($cm^3 \cdot g^{-1}$)	Average pore width (4V/S Å)
t-plot external surface area		39.50		
t-plot micropore volume			−0.000284	
BJH adsorption		36.815 [a]	0.055445 [b]	60.241
BJH desorption		37.0671 [a]	0.055555 [b]	59.950
D-H adsorption		36.726 [a]		60.238
D-H desorption		36.9780 [a]		59.943
Maximum pore volume at $p/p^\circ/cm^3/g$ (STP)			0.176986	Median pore width
			0.016283	7.736
Average particle size/Å			1515	

[a] Cumulative surface area of pores between 1.7 and 300 nm in diameter. [b] Cumulative pore volume of pores between 1.7 and 300 nm in diameter.

3.1.6. UV-Vis Diffuse Reflectance Spectroscopy

The UV-Vis DRS spectra of TiO_2-P25 and the prepared photocatalysts are shown in Figure 6a. The absorption band of TiO_2-P25, occurring from 200 to 380 nm, is associated with the O^{2-} (2p) → Ti(IV) (3d) transitions and tetrahedral symmetry [52]. In the case of Co(II)-doped TiO_2 samples, band tailing appears at ca. 400 nm; such light absorption increase in the Vis region, as compared to pure TiO_2-P25, relates to the charge transfer from O^{2-} to Co(II) [53] and to the Vis absorption of the electrons from the defect states, the intensity being directly related to the number of defect states [54]. Visible light absorption increases as less energy is required to move electrons to the conduction band. The band gap (E_g) was obtained using the Tauc plot, Figure 6b [55]. For pure TiO_2-P25, the band gap was found equal to 3.3 eV in agreement with the literature [56]. For cobalt-doped TiO_2 photocatalysts, E_g narrows and depends on Co concentration (Table 6), with values around 2.3–2.4 eV. Table S2 lists the band gap of several Co-doped TiO_2 photocatalysts. It follows that the band gap depends on the synthetic method and on the nature of the starting material. The E_g narrowing, observed as an absorption onset shift to the visible region, is due both to the substitution of Ti(IV) by Co(II), which implies new d-states coming from Co- in the forbidden band of TiO_2, and to the addition of energy levels in the same zone from oxygen vacancies [36].

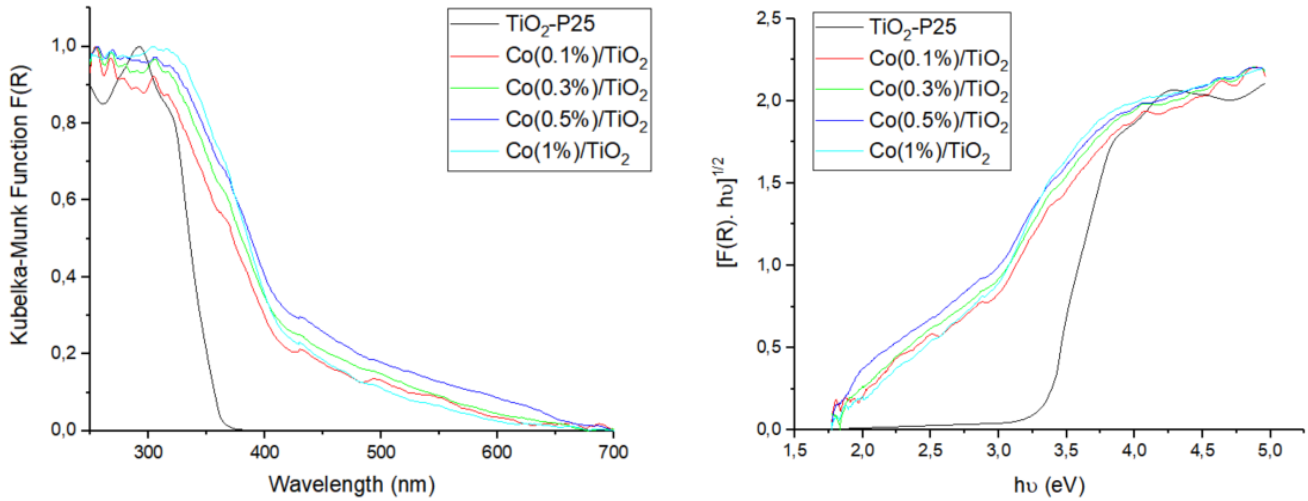

Figure 6. UV-Vis diffuse reflectance spectra of pure TiO_2-P25 and Co/TiO_2 samples (**a**) Kubelka–Munk; (**b**) Tauc plot (indirect band gap).

Table 6. Band gap of TiO_2-P25 and Co-doped TiO_2 samples and pseudo first order rate constants for phenol degradation under NUV-Vis and UV irradiation. [Phenol] = 50 mg·L^{-1}; Photocatalyst = 1g·L^{-1}, T ca. 25 °C, natural pH.

Photocatalyst	Indirect Eg (eV)	Vis		UV	
		$k \cdot 10^2$ (min^{-1})	R^2	$k \cdot 10^2$ (min^{-1})	R^2
TiO_2-P25	3.3	0.060 ± 0.002	0.90	3.6 ± 0.8	0.97
0.1% Co/TiO_2	2.4	1.1 ± 0.2	0.98	4.5 ± 0.7	0.96
0.3% Co/TiO_2	2.3	0.8 ± 0.2	0.98	5.2 ± 0.3	0.90
0.5% Co/TiO_2	2.3	0.41 ± 0.09	0.96	3.8 ± 0.5	0.96
1.0% Co/TiO_2	2.3	0.7 ± 0.2	0.98	5.5 ± 0.9	0.86

The presence of cobalt energy levels over the Fermi level inhibits visible-light absorption and prevents e^-/h^+ pair recombination, thus enhancing the photocatalytic efficiency, but an excess of dopant facilitates hole–electron pair recombination, reducing the photocatalytic activity [36,37].

3.2. Kinetics of Phenol Photodegradation

The photocatalytic activity of TiO_2 and Co-TiO_2-doped samples was tested by monitoring phenol photodegradation upon UV and NUV-Vis radiation. After irradiation, e^-/h^+ pairs are formed according to the usual scheme of photocatalysis with semiconductors, [57,58] and the dopant Co(II) traps e^-, thus reducing the probability of recombination. O_2 and H_2O/HO^- adsorbed onto the photocatalyst surface scavenge the trapped e^- and h^+ to form reactive oxygen species (hydroxyl, $HO^\bullet$, hydroperoxy, $HO_2^\bullet$, and superoxide, $O_2^{\bullet-}$ radicals, and H_2O_2), which are involved in the oxidative photodegradation of phenol, same as h^+.

In the case of pure TiO_2, the degradation of phenol was found to be effective under UV light, which was not the case under NUV-Vis light (Figure 7). The same results were found for the photodegradation under NUV-Vis light, of dyes [18,59], drugs [60], and phenol [19]. In fact, the large band gap of TiO_2 makes the absorption of visible light photons ineffective, minimizing its photoactivity [61].

Materials **2023**, *16*, x FOR PEER REVIEW 13 of 18
Materials **2023**, *16*, 4134 13 of 18

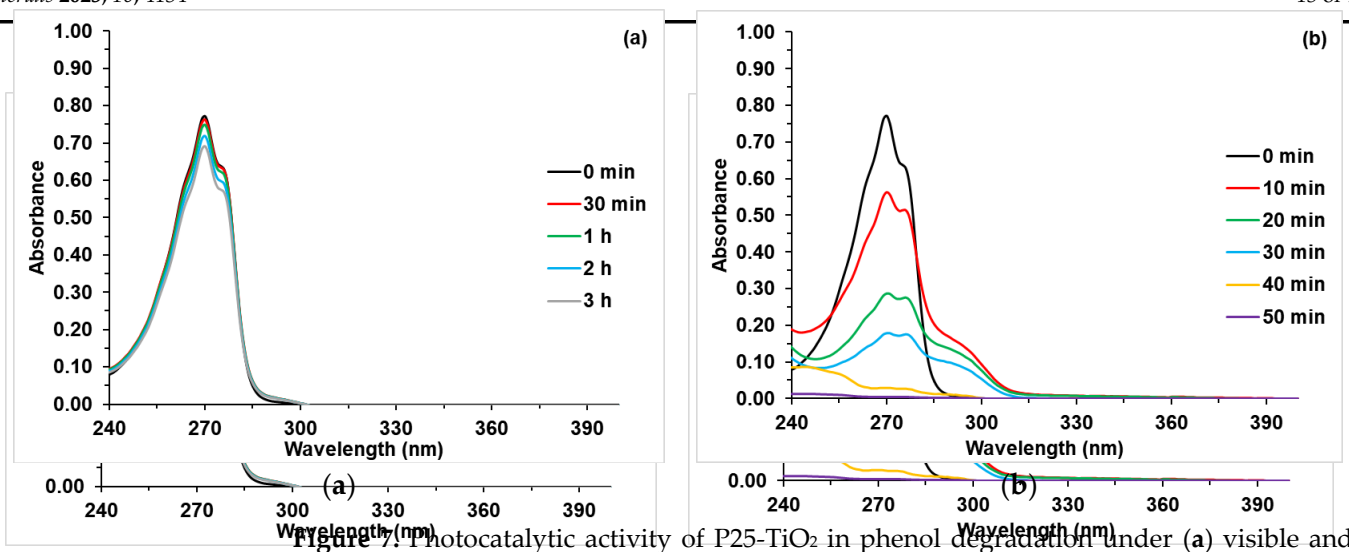

Figure 7. Photocatalytic activity of P25-TiO_2 in phenol degradation under (**a**) visible and (**b**) UV irradiation. [Phenol] = 50 mg·L^{-1}; P25-TiO_2 = 1g·L^{-1}, T ca. 25 °C, natural pH.

Figure 7. Photocatalytic activity of P25-TiO_2 in phenol degradation under (**a**) visible and (**b**) UV irradiation. [Phenol] = 50 mg·L^{-1}; P25-TiO_2 = 1g·L^{-1}, T ca. 25 °C, natural pH.

In the case of Co(X%)/TiO_2 photocatalysts, phenol photodegradation was found to be totally different from pure P25-TiO_2 (Figures S4 and S5). Figure 8 shows the absorbance *vs.* time curves for phenol photodegradation in the presence of TiO_2-P25 and Co(%)/TiO_2 photocatalysts. The as-prepared photocatalysts slightly degrade phenol under UV light, whereas complete phenol photodegradation was observed under Vis light. Table 6 summarizes the obtained pseudo first order rate constants. Although, under UV irradiation, the rate constants are higher with Co-doped TiO_2, there is only a very small phenol disappearance; a similar behavior was observed with Cu-doped titanium [32]. On the other hand, under NUV-Vis radiation, the rate constant increases when the band gap decreases, which parallels Co content.

In the case of Co(X%)/TiO_2 photocatalysts, phenol photodegradation was found to be totally different from pure P25-TiO_2 (Figures S4 and S5). Figure 8 shows the absorbance *vs.* time curves for phenol photodegradation in the presence of TiO_2-P25 and Co(%)/TiO_2 photocatalysts. The as-prepared photocatalysts slightly degrade phenol under UV light, whereas complete phenol photodegradation was observed under Vis light. Table 6 summarizes the obtained pseudo first order rate constants. Although, under UV irradiation, the rate constants are higher with Co-doped TiO_2, there is only a very small phenol disappearance; a similar behavior was observed with Cu-doped titanium [32]. On the other hand, under NUV-Vis radiation, the rate constant increases when the band gap decreases, which parallels Co content.

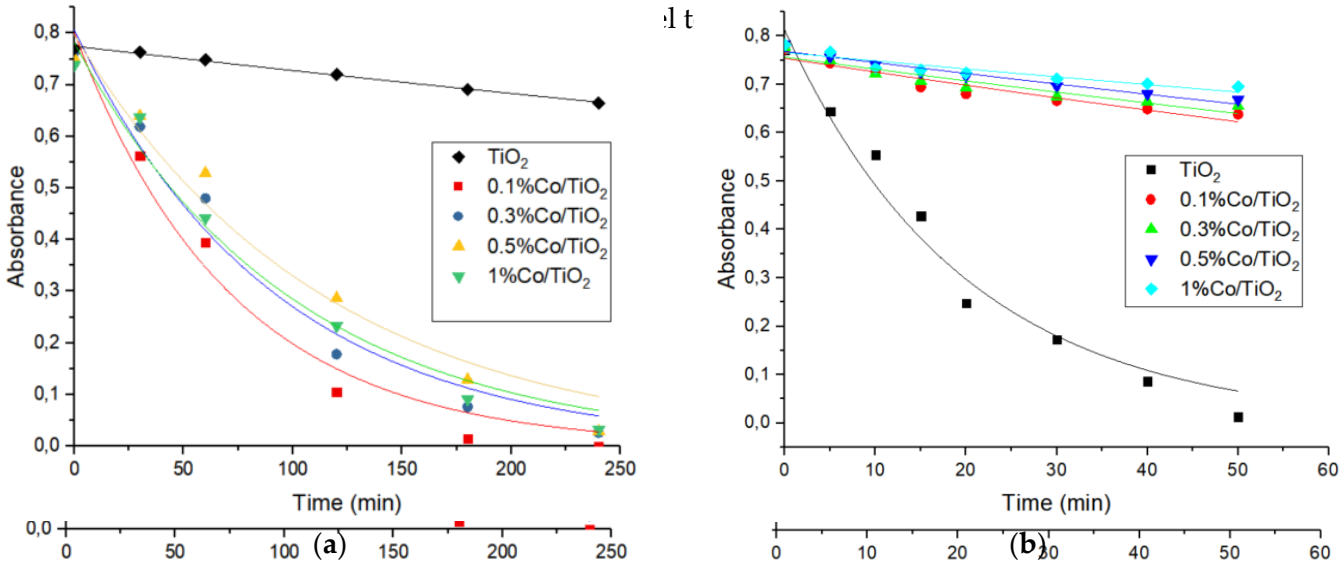

Figure 8. Absorbance vs. time curves for phenol degradation under (**a**) NUV-Vis and (**b**) UV irradiation using TiO_2-P25 and Co(X%)/TiO_2 photocatalysts. [Phenol] = 50 mg·L^{-1}; Photocatalyst = 1g·L^{-1}, T ca. 25 °C, natural pH.

Figure 8. Absorbance vs. time curves for phenol degradation under (**a**) NUV-Vis and (**b**) UV irradiation using TiO_2-P25 and Co(X%)/TiO_2 photocatalysts. [Phenol] = 50 mg·L^{-1}; Photocatalyst = 1g·L^{-1}, T ca. 25 °C, natural pH.

The photocatalytic effect was more important with the lowest concentration of doped metal, *i.e.*, Co(0.1%)/TiO_2. As stated above, the fastest phenol photodegradation happen with the Co(0.1%)/TiO_2 photocatalyst, probably due to a better dispersion of metal ions on the TiO_2-P25 surface (as found by SEM, Section 3.1.3). The same results were found by previous authors with Cu-doped titania [62]. At higher Co concentrations, the rate constants decreased slowly; in agreement with the well-known fact that above the optimal

The photocatalytic effect was more important with the lowest concentration of doped metal, *i.e.*, Co(0.1%)/TiO_2. As stated above, the fastest phenol photodegradation happen with the Co(0.1%)/TiO_2 photocatalyst, probably due to a better dispersion of metal ions on the TiO_2-P25 surface (as found by SEM, Section 3.1.3). The same results were found by previous authors with Cu-doped titania [62]. At higher Co concentrations, the rate constants decreased slowly; in agreement with the well-known fact that above the optimal

Materials **2023**, *16*, x FOR PEER REVIEW 14 of 18

decreased slowly; in agreement with the well-known fact that above the optimal value the presence of dopant reduces the photoactivity, charges are trapped and/or recombination centers are formed [25].

value the presence of dopant reduces the photoactivity, charges are trapped and/or recombination centers are formed [25].

3.3. Total Organic Carbon (TOC) Analysis

3.3. Total Organic Carbon (TOC) Analysis

To determine the degree of mineralization during photocatalysis, TOC analyses were carried out after 60 min of photoirradiation under UV light and 240 min under NUV-Vis light (Figure 9). The initial phenol concentration of 50 mg·L^{-1} with a measured TOC value of 48 mg·L^{-1} was used.

To determine the degree of mineralization during photocatalysis, TOC analyses were carried out after 60 min of photoirradiation under UV light and 240 min under NUV-Vis light (Figure 9). The initial phenol concentration of 50 mg·L⁻¹ with a measured TOC value of 48 mg·L⁻¹ was used.

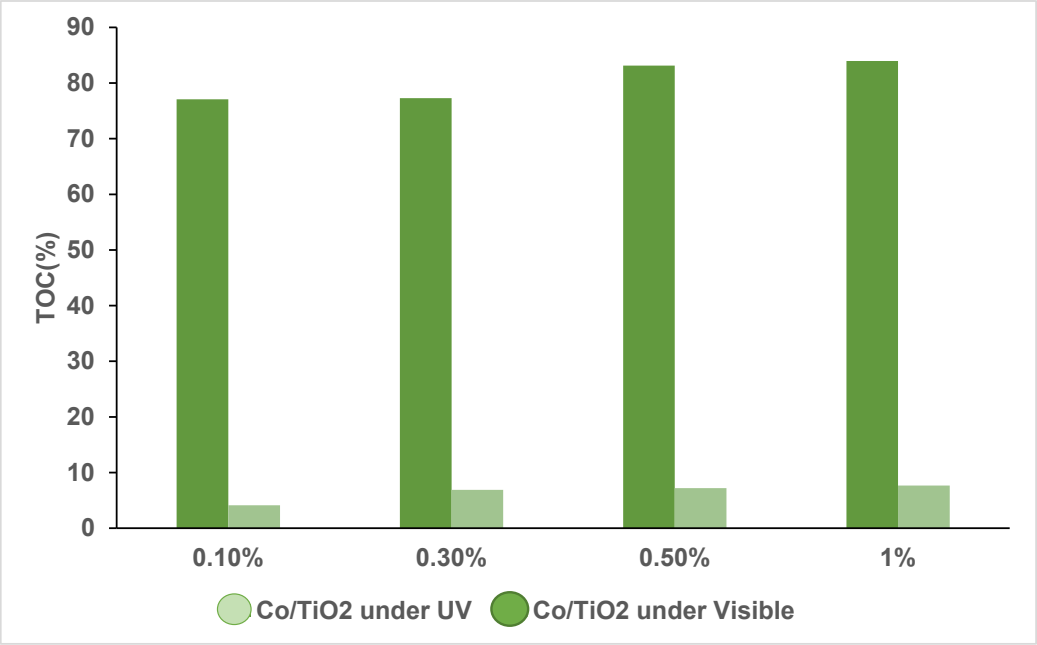

Figure 9. TOC percentage removal for phenol photodegradation using Co(X%)/TiO_2 photocatalysts. Irradiation time: NUV-Vis 240 min; UV 60 min. [Phenol] = 50 mg·L^{-1}; Photocatalysts = 1g·L^{-1}, T ca. 25 °C, natural pH.

Figure 9. TOC percentage removal for phenol photodegradation using Co(X%)/TiO_2 photocatalysts. Irradiation time: NUV-Vis 240 min; UV 60 min. [Phenol] = 50 mg·L⁻¹; Photocatalysts = 1g·L⁻¹, T ca. 25 °C, natural pH.

TOC values decreased drastically upon photocatalysis, from 48 to 1.97 mg·L^{-1} under NUV-Vis light in the presence of Co(X%)/TiO_2 photocatalysts, i.e., a 96% TOC removal, whereas the observed removal was much lower (23%) under UV light. For both irradiation conditions, the maximum TOC removal was observed for the lowest dopant content (Co(0.1%)/TiO_2), and in accordance with kinetics results, it decreased as the Co percent was increased.

TOC values decreased drastically upon photocatalysis, from 48 to 1.97 mg·L⁻¹ under NUV-Vis light in the presence of Co(X%)/TiO_2 photocatalysts, i.e., a 96% TOC removal, whereas the observed removal was much lower (23%) under UV light. For both irradiation conditions, the maximum TOC removal was observed for the lowest dopant content (Co(0.1%)/TiO_2), and in accordance with kinetics results, it decreased as the Co percent was increased.

TOC results are in agreement with kinetic results; the observed absorbance decay follows the same pattern found for TOC, irrespective of the irradiation wavelength: small decay and TOC reduction with UV and almost complete elimination with NUV-Vis.

TOC results are in agreement with kinetic results; the observed absorbance decay follows the same pattern found for TOC, irrespective of the irradiation wavelength: small decay and TOC reduction with UV and almost complete elimination with NUV-Vis.

3.4. Photodegradation and Energetic Efficiency of the Process

3.4. Photodegradation and Energetic Efficiency of the Process

Using the light intensity (I_λ/Einstein·L^{-1}·s^{-1}) at the irradiation wavelength (λ), the molar absorptivity at λ (ε_λ/mol·dm^{-3}·cm^{-1}), the pathlength of the photoreactor (l/cm), and the apparent pseudo first order rate constant (k/s^{-1}), the photocatalysis quantum yield ($\Phi_{photodegradation}$) can be calculated (Table 7) [28]; likewise, taking into account the apparent pseudo first order rate constant (k/s^{-1}), the electric power consumed by the lamp (P/kW), and the solution volume (V/L), the energy efficiency parameter (E_{EO}/kW·L^{-1}·s^{-1}), i.e., the energy required to reduce the pollutant concentration per volume and time unit, can be obtained [32] (Table 7).

Using the light intensity (I_λ/Einstein·L⁻¹·s⁻¹) at the irradiation wavelength (λ), the molar absorptivity at λ (ε_λ/mol·dm⁻³·cm⁻¹), the pathlength of the photoreactor (l/cm), and the apparent pseudo first order rate constant (k/s⁻¹), the photocatalysis quantum yield ($\Phi_{photodegradation}$) can be calculated (Table 7) [28]; likewise, taking into account the apparent pseudo first order rate constant (k/s⁻¹), the electric power consumed by the lamp (P/kW), and the solution volume (V/L), the energy efficiency parameter (E_{EO}/kW·L^{-1}·s^{-1}), *i.e.*, the energy required to reduce the pollutant concentration per volume and time unit, can be obtained [32] (Table 7).

Table 7. Photodegradation quantum yield ($\Phi_{photodegradation}$) and energy efficiency (E_{EO}) for phenol photocatalyzed degradation over Co(0.1%)/TiO_2 under UV and NUV-Vis irradiation.

Irradiation Source	UV	NUV-Vis
$\Phi_{photodegradation}$	9.77	0.67
E_{EO}/kW·L $^{-1}$·s $^{-1}$	766	156835

The large value of the UV photodegradation quantum yield suggests the contribution of secondary processes, possibly chain processes. On the other hand, EEO is much more favorable with UV radiation. At first glance, the choice would be to use UV radiation if the irradiation source is to be solely powered by electric current. The advantage of using the prepared photocatalyst, under NUV-Vis, is a much higher level of TOC removal and the use of sunlight, which would make the process more sustainable and reduce energy-associated costs.

As mentioned above (vide supra), the catalyst can be washed with no lixiviation or structural consequences after use, and when reutilized, it showed similar kinetic and TOC reduction results.

4. Conclusions

The degradation of phenol was investigated using cobalt-impregnated TiO_2 samples with different concentration, Co(X%)/TiO_2, with X = 0.1%, 0.3%, 0.5%, and 1.0%, under NUV-Vis (>366 nm) and UV (254 nm) radiation. The TiO_2-P25 surface was impregnated, and the obtained solids were characterized by XRD, Raman, XPS, SEM, EDS, and TEM. Crystallite size increased in the doped samples, where Ti(IV) was substituted by Co(II) and oxygen vacancies were created as well as interband states, which reduced the band gap as found with UV-Vis DRS measurements. The N_2 adsorption isotherm corresponds to type IV with a small H3 loop near the maximum relative pressure. The photocatalytic activity over phenol photodegradation was found to be the best for Co(0.1%)/TiO_2, at the lowest found band gap (E_g ca. 2.3–2.4 eV), when using NUV-Vis radiation. The TOC test showed an approximately complete removal (96%) for phenol photodegradation under NUV-Vis radiation and Co(0.1%)/TiO_2, while it only removed 23% under UV radiation.

In summary, we easily prepared, by impregnation, and characterized a Co- doped TiO_2 (P25) photocatalyst showing extended light harvesting into the Vis region and were able to completely photodegrade phenol in an aqueous solution (50 ppm) after 3 h under NUV-Vis irradiation. The so-prepared catalyst was found to be chemically and mechanically stable and showed similar kinetic and TOC results upon reutilization.

Supplementary Materials: The following supporting information can be downloaded at: https://www.mdpi.com/article/10.3390/ma16114134/s1, Figure S1. Diffractograms of Co(0.1%)/TiO_2, a: before leaching test, b: after leaching test. Figure S2: Raman spectra of TiO_2-P25 and Co(0.1%)/TiO_2 acquired using (a) 633 nm and (b) 785 nm excitation laser line. Figure S3. XPS spectra (a) Co 2p scan and fitting; (b) Ti 2p scan; (c) O 1s scan; (d) C 1s scan. Figure S4: Time-resolved UV-Vis spectra of phenol during its UV irradiation in the presence of (a) Co(0.1%)/TiO_2, (b) Co(0.3%)/TiO_2, (c) Co(0.5%)/TiO_2, (d) Co(1%)/TiO_2. [Phenol] = 50 ppm; Photocatalysts = 1g·L^{-1}, T ca. 25 °C, natural pH. Figure S5: Time-resolved UV-Vis spectra of phenol during Vis irradiation in the presence of (a) Co(0.1%)/TiO_2, (b) Co(0.3%)/TiO_2, (c) Co(0.5%)/TiO_2, (d) Co(1%)/TiO_2. [Phenol] = 50 ppm; Photocatalyst = 1g·L^{-1}, T ca. 25 °C, natural pH. Table S1: Raman peak centred at 143 cm^{-1} as a function of laser line and laser's power. Table S2: Band gap for TiO_2-P25 and Co doped TiO_2 photocatalysts synthesized by different methods.

Author Contributions: Conceptualization, M.E.A., J.A.S. and M.C.; Methodology, M.E.A., A.E.H., J.A.S. and M.C.; Software, J.A.S. and M.C.; Validation, L.R.-L., A.E.H., J.A.S. and M.C.; Formal analysis, S.B., L.R.-L., J.A.S. and M.C.; Investigation, S.B., L.R.-L. and M.C.; Resources, J.A.S. and M.C.; Data curation, S.B., L.R.-L., J.A.S. and M.C.; Writing—original draft, S.B., L.R.-L. and M.C.; Writing—review & editing, S.B., J.A.S. and M.C.; Visualization, S.B., J.A.S. and M.C.; Supervision,

M.E.A., A.E.H. and M.C.; Project administration, M.C.; Funding acquisition, M.C. All authors have read and agreed to the published version of the manuscript.

Funding: This research received support through grant TED2021-132667B-I00, funded by the EU NextGenerationEU/PRTR through project MCIN/AEI/10.13039/501100011033. Financial support was also provided by the regional government *Xunta de Galicia* through project GPC/ED431B 2020/52. S.B. thanks the KA-107 grant received from the EU through the Erasmus+ program for a research stay at UDC.

Conflicts of Interest: The authors declare no conflict of interest.

References

1. Ñungo-Moreno, J.; Carriazo, S.D.; Moreno, S.; Molina, R.A. Degradación fotocatalítica de fenol empleando arcillas pilarizadas con Al-Fe y Al-Cu. *Rev. Acad. Colomb. Cienc. Exact. Fis. Nat.* **2011**, *35*, 295–302.
2. Höfer, T. Tainting of seafood and marine pollution. *Water Res.* **1998**, *32*, 3505–3512. [CrossRef]
3. Michałowicz, J.; Duda, W. Phenols—Sources and Toxicity. *Pol. J. Environ. Stud.* **2007**, *16*, 347–362.
4. Ahmaruzzaman, M. Adsorption of Phenolic Compounds on Low-Cost Adsorbents: A Review. *Adv. Colloid Interface Sci.* **2008**, *143*, 48–67. [CrossRef]
5. Zularisam, A.W.; Ismail, A.F.; Salim, R. Behaviours of Natural Organic Matter in Membrane Filtration for Surface Water Treatment—A Review. *Desalination* **2006**, *194*, 211–231. [CrossRef]
6. Yu, J.; Zhao, X.; Yang, H.; Chen, X.; Yang, Q.; Yu, L. Science of the Total Environment Aqueous Adsorption and Removal of Organic Contaminants by Carbon Nanotubes. *Sci. Total Environ.* **2014**, *482–483*, 241–251. [CrossRef]
7. Barakat, M.A. New Trends in Removing Heavy Metals from Industrial Wastewater. *Arab. J. Chem.* **2011**, *4*, 361–377. [CrossRef]
8. Canle, M.L.; Santaballa, J.A.; Vulliet, E. On the Mechanism of TiO_2—Photocatalyzed Degradation of Aniline Derivatives. *J. Photochem. Photobiol. A Chem.* **2005**, *175*, 192–200. [CrossRef]
9. Sakthivel, S.; Neppolian, B.; Shankar, M.V.; Arabindoo, B.; Palanichamy, M.; Murugesan, V. Solar Photocatalytic Degradation of Azo Dye: Comparison of Photocatalytic Efficiency of ZnO and TiO_2. *Sol. Energy Mater. Sol. Cells* **2003**, *77*, 65–82. [CrossRef]
10. Mishra, M.; Chun, D. Applied Catalysis A: General α-Fe_2O_3 as a Photocatalytic Material: A Review. *Appl. Catal. A Gen.* **2015**, *498*, 126–141. [CrossRef]
11. Alshorifi, F.T.; Alswat, A.A.; Mannaa, M.A.; Alotaibi, M.T.; E-Bahy, S.M.; Salama, R.S. Facile and Green Synthesis of Silver Quantum Dots Immobilized onto a Polymeric CTS-PEO Blend for the Photocatalytic Degradation of p-Nitrophenol. *ACS Omega* **2021**, *6*, 30432–30441. [CrossRef]
12. Alshorifi, F.T.; Alswat, A.A.; Salama, R.S. Gold-selenide Quantum Dots Supported onto Cesium Ferrite Nanocomposites for the Efficient Degradation of Rhodamine B. *Heliyon* **2022**, *8*, E09652. [CrossRef]
13. Saleh, T.S.; Badawi, A.K.; Salama, R.S.; Mostafa, M.M.M. Design and Development of Novel Composites Containing Nickel Ferrites Supported on Activated Carbon Derived from Agricultural Wastes and Its Application in Water Remediation. *Materials* **2023**, *16*, 2170. [CrossRef]
14. Miwa, T.; Kaneco, S.; Katsumata, H.; Suzuki, T. Photocatalytic Hydrogen Production from Aqueous Methanol Solution with $CuO/Al_2O_3/TiO_2$ Nanocomposite. *Int. J. Hydrog. Energy* **2010**, *35*, 6554–6560. [CrossRef]
15. Su, R.; Bechstein, R.; Sø, L.; Vang, R.T.; Sillassen, M.; Palmqvist, A.; Besenbacher, F. How the Anatase-to-Rutile Ratio Influences the Photoreactivity of TiO_2. *J. Phys. Chem. C* **2011**, *115*, 24287–24292. [CrossRef]
16. Hanaor, D.A.H.; Sorrell, C.C. Review of the Anatase to Rutile Phase Transformation. *J. Mater. Sci.* **2011**, *46*, 855–874. [CrossRef]
17. Ohno, T.; Sarukawa, K.; Tokieda, K.; Matsumura, M. Morphology of a TiO_2 photocatalyst (Degussa, P-25) Consisting of Anatase and Rutile Crystalline Phases. *J. Catal.* **2001**, *203*, 82–86. [CrossRef]
18. Kouamé, N.A.; Alaoui, O.T.; Herissan, A.; Larios, E.; José-Yacaman, M.; Etcheberry, A.; Colbeau-Justin, C.; Remita, H. Visible Light-Induced Photocatalytic Activity of Modified Titanium(IV) Oxide with Zero-Valent Bismuth Clusters. *New J. Chem.* **2015**, *39*, 2316–2322. [CrossRef]
19. Hai, Z.; El Kolli, N.; Uribe, D.B.; Beaunier, P.; José-Yacaman, M.; Vigneron, J.; Etcheberry, A.; Sorgues, S.; Colbeau-Justin, C.; Chen, J.; et al. Modification of TiO_2 by Bimetallic Au–Cu Nanoparticles for Wastewater Treatment. *J. Mater. Chem. A* **2013**, *1*, 10829–10835. [CrossRef]
20. Boukhatem, H.; Khalaf, H.; Djouadi, L.; Gonzalez, F.V.; Navarro, R.M.; Santaballa, J.A.; Canle, M. Photocatalytic Activity of Mont-La (6%)-Cu0.6Cd0.4S Catalyst for Phenol Degradation under near UV Visible Light Irradiation. *Appl. Catal. B Environ.* **2017**, *211*, 114–125. [CrossRef]
21. Grabowska, E.; Reszczyńska, J.; Zaleska, A. Mechanism of Phenol Photodegradation in the Presence of Pure and Modified-TiO_2: A Review. *Water Res.* **2012**, *46*, 5453–5471. [CrossRef] [PubMed]
22. Fabiano, M.; Almeida, D.; Roberto, C.; Honor, A.; Olavo, S.; Lopes, J.; Divina, L.; Miranda, L. Applied Surface Science Enhanced Photocatalytic Activity of TiO_2—Impregnated with MgZnAl Mixed Oxides Obtained from Layered Double Hydroxides for Phenol Degradation. *Appl. Surf. Sci.* **2015**, *357*, 1765–1775. [CrossRef]
23. Dobrosz-Gómez, I.; Gómez-García, M.; López Zamora, S.M.; Gilpavas, E.; Bojarska, J.; Kozanecki, M.; Rynkowski, J.M. Transition Metal Loaded TiO_2 for Phenol Photo-Degradation. *Comptes Rendus Chim.* **2015**, *18*, 1170–1182. [CrossRef]

24. Iawasaki, T.; Hara, M.; Kawada, H.; Tada, H.; Ito, S. Cobalt Ion-Doped TiO_2 Photocatalyst Response to Visible Light. *J. Colloid Interface Sci.* **2000**, *204*, 202–204. [CrossRef] [PubMed]
25. Barakat, M.A.; Schaeffer, H.; Hayes, G.; Ismat-shah, S. Photocatalytic Degradation of 2-Chlorophenol by Co-Doped TiO_2 Nanoparticles. *Appl. Catal. B Environ.* **2005**, *57*, 23–30. [CrossRef]
26. El Mragui, A.; Zegaoui, O.; da Silva, J.C.G.E. Chemosphere Elucidation of the Photocatalytic Degradation Mechanism of an Azo Dye under Visible Light in the Presence of Cobalt Doped TiO_2 Nanomaterials. *Chemosphere* **2020**, *266*, 128931. [CrossRef]
27. El Shazly, A.N.; El Sayyad, G.S.; Hegazy, A.H.; Hamza, M.A.; Fathy, R.M.; El Shenawy, E.T.; Allam, N.K. Superior Visible Light Antimicrobial Performance of Facet Engineered Cobalt Doped—TiO_2 Mesocrystals in Pathogenic Bacterium and Fungi. *Sci. Rep.* **2021**, *11*, 5609. [CrossRef]
28. Konstantinou, I.K.; Albanis, T.A. TiO_2—Assisted Photocatalytic Degradation of Azo Dyes in Aqueous Solution: Kinetic and Mechanistic Investigations: A Review. *Appl. Catal. B Environ.* **2004**, *49*, 1–14. [CrossRef]
29. Romeiro, A.; Freitas, D.; Emília Azenha, M.; Canle, M.; Burrows, H.D. Effect of the Calcination Temperature on the Photocatalytic Efficiency of Acidic Sol-Gel Synthesized TiO_2 nanoparticles in the Degradation of Alprazolam. *Photochem. Photobiol. Sci.* **2017**, *16*, 935–945. [CrossRef]
30. Li, X.; Zou, X.; Qu, Z.; Zhao, Q.; Wang, L. Photocatalytic Degradation of Gaseous Toluene over Ag-Doping TiO_2 Nanotube Powder Prepared by Anodization Coupled with Impregnation Method. *Chemosphere* **2011**, *83*, 674–679. [CrossRef]
31. Kuhn, H.J.; Braslavsky, S.E.; Schmidt, R. Chemical Actinometry (IUPAC Technical Report). *Pure Appl. Chem.* **2004**, *76*, 2105–2146. [CrossRef]
32. Belekbir, S.; El Azzouzi, M.; El Hamidi, A.; Rodr, L.; Santaballa, J.A. Improved Photocatalyzed Degradation of Phenol, as a Model Pollutant, over Metal-Impregnated Nanosized TiO_2. *Nanomaterials* **2020**, *10*, 996. [CrossRef]
33. Jiang, X.; Manawan, M.; Feng, T.; Qian, R.; Zhao, T.; Zhou, G.; Kong, F.; Wang, Q.; Dai, S.; Pan, J.H. Anatase and Rutile in Evonik Aeroxide P25: Heterojunctioned or Individual Nanoparticles? *Catal. Today* **2018**, *300*, 12–17. [CrossRef]
34. Spurr, R.A.; Myers, H. Quantitative Analysis of Anatase-Rutile Mixtures with an X-Ray Diffractometer. *Anal. Chem.* **1957**, *29*, 760–762. [CrossRef]
35. Behnajady, M.A.; Eskandarloo, H. Silver and Copper Co-Impregnated onto TiO_2-P25 Nanoparticles and Its Photocatalytic Activity. *Chem. Eng. J.* **2013**, *228*, 1207–1213. [CrossRef]
36. Khurana, C.; Bhupendra, O.P.P. Synthesis of Visible Light-Responsive Cobalt-Doped TiO_2 Nanoparticles with Tunable Optical Band Gap. *J. Sol-Gel Sci. Technol.* **2015**, *75*, 424–435. [CrossRef]
37. Choudhury, B.; Choudhury, A. Luminescence Characteristics of Cobalt Doped TiO_2 Nanoparticles. *J. Lumin.* **2012**, *132*, 178–184. [CrossRef]
38. Scherrer, V.P. Bestimmung Der Inneren Struktur Und Der Größe von Kolloidteilchen Mittels Röntgenstrahlen. *Nachr. Ges. Wiss. Göttingen Math. Phys. Kl.* **1918**, *1918*, 98–100.
39. Busca, G.; Ramis, G.; Piaggio, P. FT Raman and FTlR Studies of Titanias and Metatitanate Powders. *J. Chem. Soc. Faraday Trans.* **1994**, *90*, 3181–3190. [CrossRef]
40. Shannon, R.D. Revised Effective Ionic Radii and Systematic Studies of Interatomic Distances in Halides and Chalcogenides. *Acta Crystallogr. A* **1976**, *32*, 751–767. [CrossRef]
41. Hardcastle, F.D.; Ishihara, H.; Biris, A.S. Photoelectroactivity and Raman spectroscopy of anodized titania (TiO_2) photoactive water-splitting catalysts as a function of oxygen-annealing temperature. *J. Mater. Chem.* **2011**, *21*, 6337–6345. [CrossRef]
42. El-Shazly, A.N.; Hegazy, A.H.; El Shenawy, E.T.; Hamza, M.A.; Allam, K. Solar Energy Materials and Solar Cells Novel Facet-Engineered Multi-Doped TiO_2 Mesocrystals with Unprecedented Visible Light Photocatalytic Hydrogen Production. *Sol. Energy Mater. Sol. Cells* **2021**, *220*, 110825. [CrossRef]
43. Gaur, L.K.; Kumar, P.; Kushavah, D.; Khiangte, K.R.; Mathpal, M.C.; Agrahari, V.; Gairola, S.P.; Soler, M.A.G.; Swart, H.C.; Agarwal, A. Laser induced phase transformation influenced by Co doping in TiO_2 nanoparticles. *J. Alloy. Compd.* **2019**, *780*, 25–34. [CrossRef]
44. Yang, L.; Qin, X.; Gong, M.; Jiang, X.; Yang, M.; Li, X.; Li, G. Molecular and Biomolecular Spectroscopy Improving Surface-Enhanced Raman Scattering Properties of TiO_2 Nanoparticles by Metal Co Doping. *Spectrochim. Acta Part A Mol. Biomol. Spectrosc.* **2014**, *123*, 224–229. [CrossRef] [PubMed]
45. Szadkowska-nicze, M.; Abramczyk, H. Raman Spectroscopy of Visible-Light Photocatalyst—Nitrogen-Doped Titanium Dioxide Generated by Irradiation with Electron Beam. *Chem. Phys. Lett.* **2013**, *566*, 54–59. [CrossRef]
46. Biesinger, M.C.; Payne, B.P.; Grosvenor, A.P.; Gerson, A.R.; Smart, R.S.C. Resolving surface chemical states in XPS analysis of first row transition metals, oxides and hydroxides: Cr, Mn, Fe, Co and Ni. *Appl. Surf. Sci.* **2011**, *257*, 2717–2730. [CrossRef]
47. Das, K.; Sharma, S.N.; Kumarm, M.; De, S.K. Morphology Dependent Luminescence Properties of Co Doped TiO_2 Nanostructures. *J. Phys. Chem. C* **2009**, *113*, 14783–14792. [CrossRef]
48. Shao, G.-S.; Zhang, X.-J.; Yuan, Z.-Y. Preparation and photocatalytic activity of hierarchically mesoporous-macroporous $TiO_{2-x}N_x$. *Appl. Catal. B Environ.* **2008**, *82*, 208–218. [CrossRef]
49. Thommes, M.; Kaneko, K.; Neimark, A.V.; Olivier, J.P.; Rodriguez-Reinoso, F.; Rouquerol, J.; Sing, K.S.W. Physisorption of Gases, with Special Reference to the Evaluation of Surface Area and Pore Size Distribution (IUPAC Technical Report). *Pure Appl. Chem.* **2015**, *87*, 1051–1069. [CrossRef]
50. Brunauer, S.; Emmett, P.H.; Teller, E. Gases in Multimolecular Layers. *J. Am. Chem. Soc.* **1936**, *60*, 309–318. [CrossRef]

51. Tianping, L.V.; Zhao, J.; Chen, M.; Shen, K.; Zhang, D.; Zhang, J.; Zhang, G.; Liu, Q. Boosted Visible-Light Photodegradation of Methylene Blue by V and Co Co-Doped TiO_2. *Materials* **2018**, *11*, 1946. [CrossRef]
52. Romeiro, A.; Azenha, M.E.; Canle, M.; Rodrigues, V.H.N.; Silva, J.P.; Burrows, H.D. Titanium Dioxide Nanoparticle Photocatalysed Degradation of Ibuprofen and Naproxen in Water: Competing Hydroxyl Radical Attack and Oxidative Decarboxylation by Semiconductor Holes. *ChemistrySelect* **2018**, *3*, 10915–10924. [CrossRef]
53. Sathish, M.; Viswanathan, B.; Viswanath, R.P.; Gopinath, C.S. Synthesis, Characterization, Electronic Structure, and Photocatalytic Activity of Nitrogen-Doped TiO_2 Nanocatalyst. *Chem. Mater.* **2005**, *17*, 6349–6353. [CrossRef]
54. Gao, L.; Li, Y.; Ren, J.; Wang, S.; Wang, R.; Fu, G.; Hu, Y. Passivation of Defect States in Anatase TiO_2 Hollow Spheres with Mg Doping: Realizing Efficient Photocatalytic Overall Water Splitting. *Appl. Catal. B Environ.* **2017**, *202*, 127–133. [CrossRef]
55. Colón, G.; Maicu, M.; Hidalgo, M.C.; Navío, J.A. Cu-Doped TiO_2 systems with Improved Photocatalytic Activity. *Appl. Catal. B Environ.* **2006**, *67*, 41–51. [CrossRef]
56. Gärtner, M.; Dremov, V.; Müller, P.; Kisch, H. Bandgap Widening of Titania through Semiconductor Support Interactions. *ChemPhysChem* **2005**, *6*, 714–718. [CrossRef]
57. Canle, M.; Fernández, M.I.; Martínez, C.; Santaballa, J.A. Photochemistry for Pollution Abatement. *Pure Appl. Chem.* **2013**, *85*, 1437–1449. [CrossRef]
58. Canle, M.; Fernández, M.I.; Martínez, C.; Santaballa, J.A. (Re)Greening Photochemistry: Using Light for Degrading Persistent Organic Pollutants. *Rev. Environ. Sci. Biotechnol.* **2012**, *11*, 213–221. [CrossRef]
59. Jaimy, K.B.; Ghosh, S.; Sankar, S.; Warrier, K.G.K. An Aqueous Sol–gel Synthesis of Chromium(III) Doped Mesoporous Titanium Dioxide for Visible Light Photocatalysis. *Mater. Res. Bull.* **2011**, *46*, 914–921. [CrossRef]
60. Martínez, C.; Canle, M.L.; Fernández, M.I.; Santaballa, J.A.; Faria, J. Applied Catalysis B: Environmental Kinetics and Mechanism of Aqueous Degradation of Carbamazepine by Heterogeneous Photocatalysis Using Nanocrystalline TiO_2, ZnO and Multi-Walled Carbon Nanotubes—Anatase Composites. *Appl. Catal. B Environ.* **2011**, *102*, 563–571. [CrossRef]
61. Ohno, T.; Akiyoshi, M.; Umebayashi, T.; Asai, K.; Mitsui, T.; Matsumura, M. Preparation of S-Doped TiO_2 Photocatalysts and Their Photocatalytic Activities under Visible Light. *Appl. Catal. A Gen.* **2004**, *265*, 115–121. [CrossRef]
62. Nasution, H.W.; Purnama, E.; Kosela, S.; Gunlazuardi, J. Photocatalytic Reduction of CO_2 on Copper-Doped Titania Catalysts Prepared by Improved-Impregnation Method. *Catal. Commun.* **2005**, *6*, 313–319. [CrossRef]